

Cooperative 3D Beamforming for Small-Cell and Cell-Free 6G Systems

Sarath Gopi, Sheetal Kalyani and Lajos Hanzo

Abstract—Three dimensional (3D) resource reuse is an important design requirement for the prospective 6G wireless communication systems. Hence, we propose a cooperative 3D beamformer for use in 3D space. Explicitly, we harness multiple base station antennas for joint zero forcing transmit pre-coding for beaming the transmit signals in specific 3D directions. The technique advocated is judiciously configured for use in both cell-based and cell-free wireless architectures. We evaluated the performance of the proposed scheme using the novel metric of Volumetric Spectral Efficiency (VSE). We also characterized the performance of the scheme in terms of its spectral efficiency (SE) and Bit Error Rate (BER) through extensive simulation studies.

I. INTRODUCTION

Industrial as well as academic research groups and standard bodies have embarked on studying the technical requirements of 6G systems. In contrast to 5G, 6G is expected to connect “intelligence”, rather than just “things”, while satisfying more stringent energy efficiency, latency and rate targets. Diverse technologies, such as Terahertz solutions, cell free massive MIMO, 3D spatial modulation as well as the Internet of “nano and bio things”, have been recommended for use in 6G systems [1]–[5].

Given the recent advances of non-terrestrial communication relying on unmanned arial vehicles (UAVs) such as drones, airships and balloons, 6G is expected to harness them for enhancing both the coverage quality and capacity [6]–[9]. Explicitly, when mmWave and Terahertz frequencies are used, only Line-of-Sight (LOS) communication is feasible owing to the high probability of blockage. Hence, the assistance of UAVs will become inevitable to provide services to users, where conventional terrestrial network is unavailable. These UAVs may play the role of both user equipment (UE) and of arial base stations (BS). These air-born UEs coexist with terrestrial ground users and are often termed as cellular-connected UAVs, which have been harnessed in applications such as remote sensing [10], [11], package delivery [12], surveillance [13] etc. A direct consequence of this new paradigm is that the UEs and BSs are going to co-exist in 3D space, where many of these have to engage in simultaneous communications.

Therefore, in 6G systems, the provision of services for arial users at different altitude is also expected to

become a requirement. In this context, both the volumetric spectral-efficiency and energy-efficiency become important new performance metrics. Hence, the 3D reuse of communication resources is expected to become an important differentiator between 5G and 6G [14]. In support of the associated 3D resource allocation, we propose a novel 3D beamforming technique, which is capable of beneficially focussing the transmit signal in 3D space so that the spectral resources can be efficiently reused without excessive interference.

A typical communication scenario showing the difference of the proposed beamforming techniques with respect to conventional 2D and 3D beamforming is portrayed in Fig 1. Four UEs are shown in Fig. 1, where $UE1$ and $UE2$ are terrestrial users, while $UE3$ and $UE4$ are arial users. All the four UEs have the same azimuth angle with respect to the antenna array (AA) $A1$. Hence, a conventional 2D beamformer will be unable to separate them in the angular domain. Now, $UE1$ and $UE3$ have the same elevation angle with respect to $A1$, whereas the elevation angle of $UE2$ and $UE4$ is different from that of $UE1$ and $UE3$. Therefore, a 3D beamformer [15], [16] is indeed capable of distinguishing $UE1$ and $UE3$ from $UE2$ and $UE4$ in the angular domain. However, $UE1$ and $UE3$, as well as $UE2$ and $UE4$ cannot be separated even with the aid of 3D beamforming, because they have identical azimuth and elevation angles. Hence, we propose cooperative beamforming, which exploits a pair of AAs, namely $A1$ and $A2$ at the right of Fig. 1. Hence, each fraction of the 3D space can be uniquely targeted. Therefore, all four UEs of Fig. 1 can simultaneously communicate using cooperative 3D beamforming.

In addition to the UAV assisted scenario of Fig.1, the proposed scheme may also be readily used for supporting the Internet of Things (IoT). The evolution of IoT extended the application of wireless communications from smartphones and tablets to smart wearable, live health monitoring systems and diverse other sensors, which have new applications in agriculture, water supply and the smart grid [17]–[20]. These applications support users in 3D space, especially in dense multi-story buildings of an urban scenario, while requiring a high data rate and ultra-low latency. Hence, our cooperative 3D beamforming technique becomes beneficial in such a scenario.

A compelling technology for next generation wire-

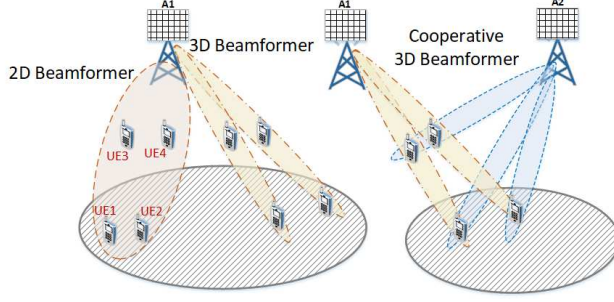


Fig. 1: Difference between conventional 2D & 3D beamformer and the proposed cooperative 3D beamformer.

less communication systems is constituted by massive multiple-input multiple-output (Massive MIMO) systems, where both the base station and the users have numerous antennas [21], [22], hence exhibiting much improved throughput, energy efficiency, and reduced interference [23]. We can have either collocated or distributed massive MIMO architectures. It has been shown in [24] that a distributed MIMO scheme achieves better coverage quality than its collocated counterpart owing to its improved diversity gain. A distributed architecture, where the antennas are geographically separated, acts as a MIMO network and it is also termed as a virtual MIMO or distributed antenna system (DAS) [25]–[29]. For exploiting the advantages of distributed systems, a cell-free architecture has been proposed in [30] for next generation wireless communication, because it has been shown to outperform the maturing small-cell systems. To weigh up the associated pros and cons, we consider our proposed scheme in both small-cell and cell-free architectures.

Our main contributions are:

- We propose a cooperative 3D beamforming (CBF) technique, relying on position based transmit beamforming (PBTBF). As demonstrated in Fig. 1, this is quite different from conventional 3D beamforming, where a single AA is used to form a sharp transmit beam in some specific azimuth and elevation angle pair. We may also refer to our cooperative 3D beamforming scheme as joint transmit pre-coding (TPC) relying on a pair of AAs to focus the transmit signal into the specified 3D region and thereby assist in simultaneously serving the user in any 3D space, which is one of the 6G design requirements. Since 6G itself is in its planning phase, we believe that our proposal is the first of its kind.
- We define a novel metric termed as the average Volumetric Spectral Efficiency (VSE) for quantifying the performance of the proposed scheme. Explicitly, the VSE is defined as the sum of the maximum average number of bps/Hz/km³. This is the 3D dual pair of the average Area Spectral

Efficiency (ASE) metric of Alouni and Goldsmith [31], which has been widely used as a performance metric in terrestrial communication [32]–[35]. Similarly to the 2D ASE of conventional cellular systems, the 3D VSE captures the trade-off between the frequency reuse factor and the resultant link quality offered to the users. Hence, it will assist in the optimal allocation of resources in 6G systems.

- The proposed CBF technique may rely on both collocated AAs and on distributed antennas, hence it is beneficial for both small-cell and cell-free architectures. We demonstrate how to make this 3D resource reuse possible in both cell-free as well as small-cell architectures and study the impact of these architectures in the context of VSE.
- We derive the mathematical expression for the VSE of the proposed scheme, which is also characterized by extensive simulation results and compared to the corresponding theoretical results.

The proposed scheme can also be used both at mmWave and the Terahertz frequencies, hence it is beneficial for 6G systems. A significant advantage of our proposed scheme is that the transmitter does not have to rely on any channel knowledge for pre-coding, rather it simply relies on the user positions. In Section II, we develop the proposed CBF technique. The performance metric VSE is defined and derived in Section III. Our simulation results are detailed in Section IV, and the paper is concluded in Section V.

II. PROPOSED SCHEME

The basic idea of the proposed scheme is discussed using Fig. 2. Let us assume having a pair of AAs A1 and A2, each having M elements, where A1 and A2 are separated in 3D space and the users are spatially distributed in 3D all around these AAs. It is assumed that each UE has a single antenna. Let us assume that UE0 is the user of interest, located at the 3D angles of θ_{L0} and θ_{R0} with respect to AAs A1 and A2, respectively. Here $\theta_{L0} = (\theta_{L0}^H, \theta_{L0}^V)$ is the azimuth-elevation angle pair of A1 and similarly $\theta_{R0} = (\theta_{R0}^H, \theta_{R0}^V)$ is that of A2. UE0 is shown to be an aerial user in Fig. 2 with $X'O'Y'$ being a horizontal plane parallel to the ground plane XOY . We consider the case, where there are many interferers and these can be located anywhere in space. However, we specifically consider the pair of interferers UE1 and UE2 in Fig. 2. Here, UE1 has the same 3D angle as that of UE0, i.e., θ_{L0} with respect to A1, whereas the 3D angle of UE2 with respect to A2 is θ_{R0} , which is the same as that of UE0. Hence, a conventional 3D beamformer using either A1 or A2 fails to simultaneously communicate with these three users. However, the interference emanating from users, who do not have the same 3D angle as that of the desired user can be readily eliminated using conventional 3D beamforming or zero-forcing TPC

by a single AA [36]–[39]. For example, in Fig. 2 transmission to both $UE1$ and $UE0$ can be arranged simultaneously using conventional 3D beamforming at AA $A2$. However, our 3D CBF technique is required for simultaneous transmission to all of $UE0$, $UE1$ and $UE2$ in Fig.2.

In order to elaborate further on the proposed 3D CBF scheme, we make the following assumptions:

- 1) Each AA knows the locations of the other AA and all users. Furthermore, they know the information to be transmitted to the user.
- 2) Perfect synchronization exists between two AAs.
- 3) Each user has the perfect knowledge of its channel from both AAs as well as the locations of both AAs. However, note that only the user needs the channel information for decoding, whereas the AAs only require location information for precoding.
- 4) A strong line-of-sight (LOS) path exists between each and every user, hence we have Rician channels between the AA and the user.

Note that the above assumptions may indeed be satisfied in practise. For example, a base station controlling the two antenna arrays can share information among them and synchronize them. A fibre link between the AAs can also be used to achieve this. In any communication system, the channel information is essential for detecting the symbols and can be acquired by channel estimation. However, in our case, the users have to estimate two channels, namely between themselves and the pair of AAs. Finally, it is widely recognized that a strong LOS path is necessary for reliable communication at mmWave and Terahertz frequencies [2], [40], [41]. In the proposed scheme, we use antenna arrays to form beams towards the user and thereby rely on a LOS path. Let us now detail the proposed 3D CBF scheme.

Let s_0 be the desired signal to be transmitted to $UE0$. Let us assume furthermore that this signal is transmitted from both AAs $A1$ and $A2$ by the TPC vector \mathbf{e}_0 . Let \mathbf{h}_{L0} and \mathbf{h}_{R0} be the channel vector between $A1$ and $UE0$ and $A2$ and $UE0$, respectively. As stated in assumption (4), both \mathbf{h}_{L0} and \mathbf{h}_{R0} are represented by Rician channels. Then the signal received at $UE0$ in the absence of any other user is given by:

$$\mathbf{y}_1 = (\mathbf{h}_{L0} + \mathbf{h}_{R0})^H \mathbf{e}_0 s_0 + n_0. \quad (1)$$

Let us assume that there are N interferers, with $s_n, 1 \leq n \leq N$ being the symbols to be transmitted to the n^{th} UE and let \mathbf{e}_n be the corresponding TPC vector. Hence, the received signal of $UE0$ is given by:

$$y_1 = (\mathbf{h}_{L1} + \mathbf{h}_{R1})^H \left(\sum_{n=0}^N \mathbf{e}_n s_n \right) + w_0, \quad (2)$$

where $n = 0$ corresponds to the terms related to the desired user and $w_0 \sim \mathcal{CN}(0, \sigma^2)$ is the AWGN component. Let \mathbf{e}_{Ln} and \mathbf{e}_{Rn} represent the position-based steering vectors of the n^{th} UE with respect to

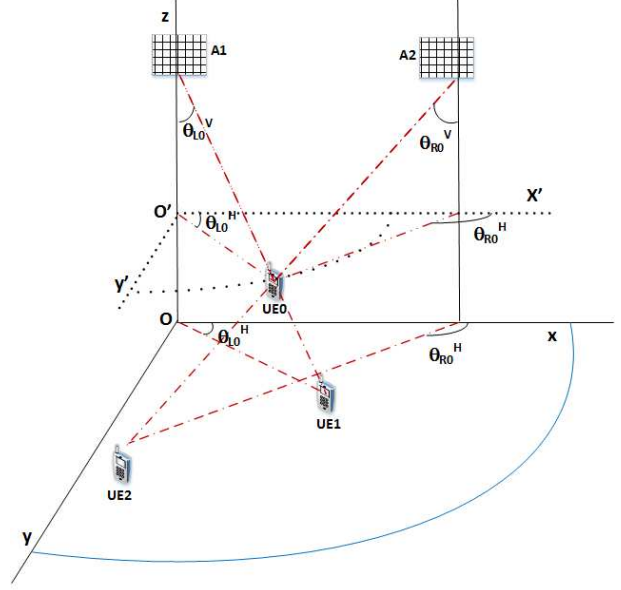


Fig. 2: The 3D geometry considered.

AAs $A1$ and $A2$, respectively. Explicitly, \mathbf{e}_{Ln} and \mathbf{e}_{Rn} are $M \times 1$ vectors, whose i^{th} entry is of the form $\exp[j\frac{2\pi}{\lambda}(x_i\psi_n^x + y_i\psi_n^y + z_i\psi_n^z)]$. Here, for \mathbf{e}_{Ln} , we have $\psi_n^x = \sin\theta_{Ln}^V \cos\theta_{Ln}^H$, $\psi_n^y = \sin\theta_{Ln}^V \sin\theta_{Ln}^H$ and $\psi_n^z = \cos\theta_{Ln}^V$. Similarly, for \mathbf{e}_{Rn} , the corresponding values are $\psi_n^x = \sin\theta_{Rn}^V \cos\theta_{Rn}^H$, $\psi_n^y = \sin\theta_{Rn}^V \sin\theta_{Rn}^H$ and $\psi_n^z = \cos\theta_{Rn}^V$, where (x_i, y_i, z_i) represents the corresponding coordinate of the i^{th} element in $A1$ and $A2$ respectively, for \mathbf{e}_{Ln} and \mathbf{e}_{Rn} . Therefore, \mathbf{h}_{L0} and \mathbf{h}_{R0} can be written under the Rician channel model as [42]:

$$\mathbf{h}_{L0} = \sqrt{\frac{K}{K+1}} \mathbf{e}_{L0} + \sqrt{\frac{1}{K+1}} \mathbf{h}_L \quad (3)$$

and

$$\mathbf{h}_{R0} = \sqrt{\frac{K}{K+1}} \mathbf{e}_{R0} + \sqrt{\frac{1}{K+1}} \mathbf{h}_R, \quad (4)$$

where the first term at the RHS of (3) and (4) is the LOS component, while \mathbf{h}_L and \mathbf{h}_R represent the nonLOS components. Furthermore it is assumed that each entry of \mathbf{h}_L and \mathbf{h}_R is an i.i.d zero mean complex Gaussian random variable. Let $\mathbf{h}_0 = \mathbf{h}_{L0} + \mathbf{h}_{R0}$.

Now, we propose to select the position-based joint TPC (JTPC) vector \mathbf{e}_0 as the solution of the following optimization problem.

$$\begin{aligned} \min_{\mathbf{e}_0} \quad & \|\mathbf{e}_0 - (\mathbf{e}_{L0} + \mathbf{e}_{R0})\|^2 \\ \text{such that } & \mathbf{e}_0^H (\mathbf{e}_{Ln} + \mathbf{e}_{Rn}) = 0 \\ & \text{for each interferer } n = 1, 2, \dots, N. \end{aligned} \quad (5)$$

The solution of (5) is [43, pp. 169]:

$$\mathbf{e}_0 = \left(\mathbf{I} - \mathbf{E}_0 (\mathbf{E}_0^H \mathbf{E}_0)^{-1} \mathbf{E}_0^H \right) (\mathbf{e}_{L0} + \mathbf{e}_{R0}), \quad (6)$$

where \mathbf{E}_0 is the matrix whose columns are $(\mathbf{e}_{Ln} + \mathbf{e}_{Rn}), n = 1, \dots, N$. Note that the solution

of (5) is the zero-forcing JTPC vector for the space spanned by $(\mathbf{e}_{L0} + \mathbf{e}_{R0})$, whose response is zero in the space spanned by $(\mathbf{e}_{Ln} + \mathbf{e}_{Rn})$ for $n \neq 0$. Similarly, the JTPC vector for each user may also be readily computed. Note that the JTPC vector \mathbf{e}_0 of (6) completely cancels the contributions of all LOS components of the interferers. Now in Section II-A and II-B, the specific small-cell and cell-free scenarios are discussed.

A. Small-Cell Architecture

In small-cell based systems, the AAs $A1$ and $A2$ of Fig. 2 can be a pair of cooperating BSs, each equipped with M -element AAs. However, the concept is not restricted to a twin BS configurations, it can also work for more complex BS configurations. For example, a single BS having two antennas, which are sufficiently separated can also be used. Another option is to have a single transmit antenna cooperating with a pair of Reconfigurable Intelligent Surfaces (RIS) controlled by a BS. Explicitly, a RIS is an array of passive reflecting elements relying on low-complexity integrated electronics for introducing a beneficial phase shift to the incident waves [44]–[46]. This has been advocated as a low-cost, energy-efficient solution for a diversity of applications [47]–[55] and can be used to provide the necessary phase shifts for the proposed scheme.

Fig. 3 shows the example of a 3D cellular structure. The AAs $A1$ and $A2$ are intended to serve a large volume, which can be considered as a 3D macro-cell. The size of the macro-cell is limited by the maximum communication range of the AAs. This is partitioned into many small cells, termed as micro-cells, which are represented using different colours. The specific micro-cells having the same colours use the same resources. Similar to the case of existing cellular networks, the resources are shared by ensuring the same spectral resources are not used in the nearby micro-cells. In Fig. 3, the micro-cells are of cuboid shape, but can be of different shapes, such as hexagonal prisms, truncated octahedrons, rhombic dodecahedrons and so on [56]. The truncated octahedron is the closest approximation of a sphere and the number of polygons required for completely filling the 3D space is known to be the lowest for this particular structure [8], [56]. Finally, as detailed in Section II, by beneficially adjusting the phase shifts in $A1$ and $A2$, any user in the macro-cell can be served with minimal interference from other users exploiting the same resources. For example, the users $UE1$ and $UE2$ seen in Fig. 3, who have the same 3D angle as that of the AA $A1$ can be simultaneously served. Similar is the case of $UE3$ and $UE4$, which are located in the same cone of AA $A2$.

B. Cell-Free Architecture

We model our cell-free architecture as shown in Fig. 4, which is based on the one proposed in [30]

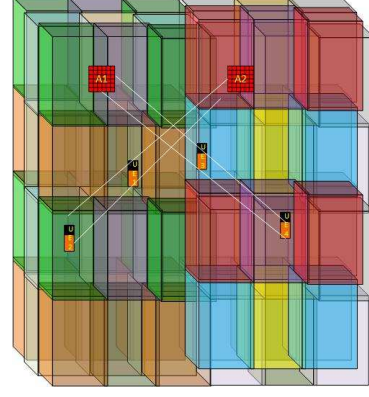


Fig. 3: Proposed architecture for small-cell system.

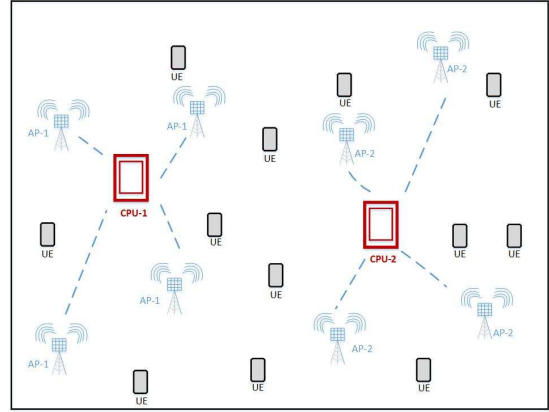


Fig. 4: Proposed architecture for cell-free system.

subject to some changes. In contrast to the small-cell based architecture, here the elements of the antenna arrays $A1$ and $A2$ are distributed throughout the cells. Specifically, the access points (APs) in Fig. 4 act as the elements in $A1$ and $A2$. In contrast to [30], the proposed cell-free architecture has the following differences.

- There are two Central Processing Units (CPU), one supporting each of the distributed antenna arrays $A1$ and $A2$.
- The antenna at the APs has more than one element. In principle, the spacing between the elements in an AA should be arranged to be less than or equal to half the wavelength of the maximum operating frequency. This condition avoids grating lobes, hence pointing the signal in the desired direction [43]. Since the APs host the geometrically separated elements of AAs, their half-wavelength spacing cannot be ensured in the distributed architecture. Hence, it is proposed to use a small AA in each of the APs, where the spacing is fixed to less than or equal to half the wavelength. Hence, in the cell-free architecture, the AAs $A1$ and $A2$ circumvent the grating lobe problem.

The entire set of APs is partitioned into two groups, each of which is associated with one of the CPUs. Note

that the number of APs associated with each CPU can be the same or different. The angle pairs θ_L and θ_R of the users are defined with respect to the two CPUs. In addition to the users' location, each AP should know the location of its respective CPU. The phase shifts to be applied at the elements of the AP to the transmit signal are calculated based on the relative positions of the corresponding CPU and the users. The basic principle is the same as that in the small-cell based architecture, except that the distributed APs act as AA A1 and A2.

The cell-free architecture is more suitable for UAV specific applications, since there may be numerous UAVs spread across the volume considered, some of which can act as APs. Now, in Section III, we will first define and then deriving the Volumetric Spectral Efficiency (VSE) of the proposed scheme.

III. VOLUMETRIC SPECTRAL EFFICIENCY

We define the average VSE as:

$$VSE = \frac{\bar{C}}{V}, \quad (7)$$

where $\bar{C} = \mathbb{E}\{\log(1 + \gamma)\}$ is the average normalized channel capacity per Hertz with γ being the Signal to Interference plus Noise Ratio (SINR) and V is the volume. Note that (7) is similar to the ASE equation [31, (8)], except that the denominator is the volume instead of the area.

Recall that the conventional terrestrial cellular structure tends to rely on perfectly tessellated hexagonal cells, which are often approximated by circles. However, in our case, the base station has to serve users in space. Hence, we propose to extend the circles to the third dimension so that the resultant spherical cellular structure covers the entire 3D user space. Hence, in this case, a BS serves the users spanned in a sphere. This can be considered as a macro-cell. Now, we partition each macro-cell into small spherical micro-cells, where the users in a micro-cell are provided with orthogonal resources. However, the same resource can be shared by the users in different micro-cells of the same macro-cell. This makes it possible to reuse the resources in a macro-cell. Let d be the diameter of the micro-cell and N_R be the reuse factor in the small-cell structure. Then the volume V is:

$$V = N_R \frac{4}{3} \pi (d/2)^3. \quad (8)$$

Note that for cell-free architectures, the denominator in (7) should be the volume of the region, where the average capacity \bar{C} is estimated divided by the number of users sharing the same resources in that region. Assuming unity power for the transmitted symbols, the instantaneous SINR can be written from (1) as:

$$\gamma = \frac{P_r \|\mathbf{h}_0^H \mathbf{e}_0\|^2}{\|\sqrt{P_r} \mathbf{h}_0^H \sum_{i=1}^N \mathbf{e}_i + \mathbf{n}_0\|^2}, \quad (9)$$

where P_r is the received signal power. We now derive the average channel capacity of the system in Theorem 1 given below.

Theorem 1. Given that the channel statistics and the desired as well as interfering users' locations are fixed, the average channel capacity per unit bandwidth is:

$$\begin{aligned} \bar{C}_{h,u} = & \frac{1}{(c_\sigma - 1) k_s^2 \log 2} e^{\frac{c_\sigma k_s^2}{1-c_\sigma}} \left(Ei \left[\frac{k_s^2}{c_\sigma - 1} \right] - Ei \left[\frac{c_\sigma k_s^2}{c_\sigma - 1} \right] \right) \\ & + \frac{1}{k_s^2 \log 2} (\gamma k_s^2 - Ei[-k_s^2] + \log(c_\sigma k_s^2) \\ & - (1 + k_s^2) (Chi(k_s^2) - Shi(k_s^2))), \end{aligned} \quad (10)$$

where $k_s = \frac{|\mu_s|}{\sigma_s}$ is the ratio of the absolute value of the average signal amplitude and its standard deviation, while $c_\sigma = \frac{\sigma_s^2}{\sigma_I^2}$ is the ratio of the variances of the signal and of the interference plus noise components. Furthermore, the notations in (10) are $Ei[x] = -\int_x^\infty \frac{e^{-t}}{t} dt$, $Chi[x] = \gamma + \log x + \int_0^x \frac{(\cosh(t)-1)}{t} dt$ and $Shi[x] = \int_0^x \frac{\sinh(t)}{t} dt$, which represent the Exponential integral, Cosh integral and Sinh integral, respectively with $\gamma \approx 0.577$ being the Euler-Mascheroni constant [57, p. 278].

Proof. See Appendix A for proof. \square

Corollary 1. When we have $k_s \gg 1$ and $c_\sigma \ll k_s^2$, the average capacity per unit bandwidth for the system can be approximated as:

$$\bar{C}_{h,u} \approx \frac{1}{\log 2} \left(\gamma + \log c_\sigma + 2 \log k_s - \frac{(c_\sigma - 1)}{c_\sigma k_s^2} \right), \quad (11)$$

Proof. See Appendix B for proof. \square

When the line-of-sight (LOS) component of the signal is sufficiently strong, i.e. $K \gg 1$, the condition $k_s \gg 1$ of Corollary 1 is satisfied. Please refer to Lemma 1 in Appendix C. In general the condition $c_\sigma \ll k_s^2$ cannot be ensured. However, note that we have $c_\sigma = \frac{\|\mathbf{e}_0\|^2}{\|\sum_{i=1}^N \mathbf{e}_i\|^2 + \frac{K+1}{2P_r} \sigma^2}$, hence when N is large, with a high probability, we have $c_\sigma < 1$. Hence, in most practical cases the approximation in Corollary 1 can be used for estimating $\bar{C}_{h,u}$. Thus Corollary 1 is beneficial, because it is numerically stable and simpler than (10). Therefore, it can be used for calculating the average channel capacity, whenever the conditions of Corollary 1 are satisfied.

Finally, the average capacity per unit bandwidth can be found by integrating (11) over all possible user and interference locations (u) and is formulated as:

$$\bar{C} = \int \bar{C}_{h,u} f_u(u) du, \quad (12)$$

where $f_u(u)$ is the distribution of the desired and interfering users' location. Note that (12) represents a multi-dimensional integral over all the possible desired and interfering user locations. The integral in (12) cannot be solved analytically, but it can be evaluated

by using Monte Carlo simulations. Finally, substituting (12) into (7) will give the average VSE of the proposed scheme. In Section IV, the VSE obtained through simulations is compared against the theoretical VSE of (7).

IV. SIMULATION RESULTS

The proposed 3D CBF technique has been evaluated through extensive simulation studies. We characterized these techniques in terms of its average VSE in $\text{bps}/\text{Hz}/\text{km}^3$, its spectral efficiency (SE) in bps/Hz and its Bit Error Rate (BER). Even though the VSE and SE are computed from the same quantity, they have different implications. For example, for a given number of users, the SE is increased as the volume is increased due to the reduction of the interference, while the VSE may increase or decrease. The VSE may be conveniently used for determining the optimal number of users in a given volume or the optimal volume for a given number of users. On the other hand, the SE quantifies the maximum total information rate in a given scenario. Therefore, the SE is useful for comparing two schemes, once the frequency-reuse topology is fixed, whereas the VSE is critical for determining the resource-reuse topology. Fig. 5 and Fig. 6 show the results of the proposed scheme for our small-cell based architecture, whereas Fig. 7-Fig. 9 characterize the cell-free architecture. Finally, in Fig. 11-Fig. 13, we compare the small-cell and cell-free architecture relying on the proposed scheme.

We consider a $500\text{ m} \times 500\text{ m} \times 120\text{ m}$ space for all simulation studies. The height is fixed to 120 m , which is the maximum allowable height for UAVs without any permit in many of the countries [7]. The simulations are carried out at millimeter wave frequencies and the parameters are chosen from [41], [58]–[61], which are reproduced below in Table I. The path loss is governed by the equation $PL = 32.4 + 20 \log d + 20 \log f$, where d is the distance and f is the carrier frequency in GHz [62]. The transmitter antenna gain is fixed to $10 \log M$, where M is the total number of elements in the antenna [63, (6-49)].

Parameter	Value
Frequency (GHz)	73.5
Bandwidth (GHz)	5
TxPower (dBm)	14.6
Other Loss (dB)	12.7
Rx Gain (dBi)	27
Rx NF (dBm)	7
Rx Noise (dB)	-76.8
Modulation	64QAM

TABLE I: Simulation parameters

We consider a spherical 3D cellular structure for evaluating the performance of the small-cell architecture. The BS's pair of transmit AAs have been placed at 120 m height separated by 120 m distance. Both these AAs have planar layout in the $x - y$ plane

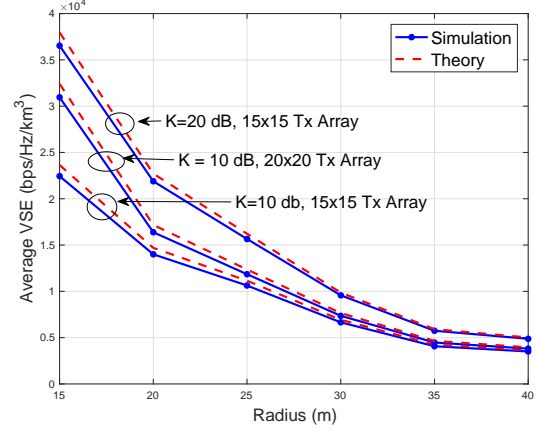


Fig. 5: Average VSE vs Cell Radius.

looking downwards. We considered both 15×15 and 20×20 AAs. The radius of the micro-cell is varied from 15 m to 40 m . The macro-cells are grouped in such a way that two cells sharing the resources are located at least a distance of four times the micro-cell radius. Hence, the number of interfering users is fixed based on the macro-cell radius. The positions of desired user and interferers are randomly selected in the respective micro-cell. The performance measures are plotted against the cell radius in Fig 5 and Fig. 6.

Fig. 5 shows the VSE of the system, where the simulation results are compared against the theoretically obtained values. Explicitly, for estimating the theoretical VSE value, we evaluated (18) theoretically and the integral in (12) is evaluated through Monte Carlo runs for various user locations. We have to bear in mind that while estimating the average VSE, the volume should be multiplied by the reuse factor in order to account for the resource reuse. Observe that the values obtained through simulations and those from theory are closely matching. It can be seen that as the cell radius increases, the average VSE decreases. As a further dominant trend, the VSE is improved as the Rician factor (K) is increased and the general VSE trend versus these parameters are as expected. Similarly, when the number of elements in the BS AA is increased, this improves the interference rejection capability, hence improving the VSE.

In Fig. 6, the average spectral efficiency (SE) in bps/Hz is plotted against the cell radius, which is calculated using (12). The theoretical values are compared against those obtained through the simulations and it can be seen that these values exhibits similar trends. In contrast to the VSE, the SE is increased with cell radius and it is improved both with K and with the number of elements in the BS AAs.

Next, the performance of the proposed scheme quantified in the cell-free architecture is considered. The users are randomly located in the $500 \times 500 \times 120\text{ m}$ space specified. Note that here all users have access to all resources. The performance is studied for different

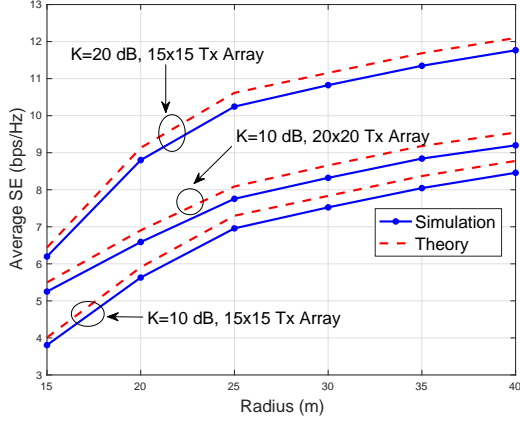


Fig. 6: Average SE vs Cell Radius.

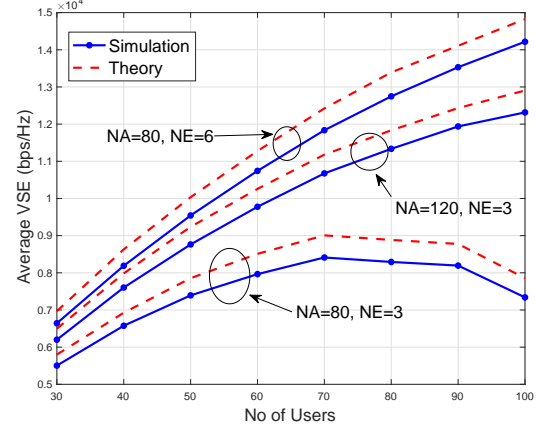


Fig. 9: Average VSE vs No of Users.

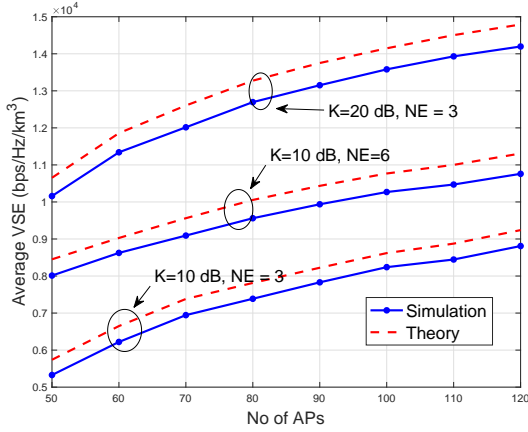


Fig. 7: Average VSE vs No of APs.

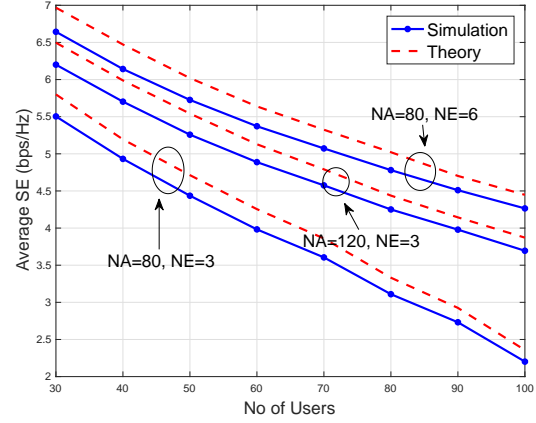


Fig. 10: Average SE vs No of Users.

number of access points (NA), number of elements per access points (NE) and number of users (NU).

In Fig. 7, the average VSE is plotted against the NA, whereas the corresponding average SE vs. NA is shown in Fig. 8 for various Rician factors and NE. It can be seen that both the average VSE and the

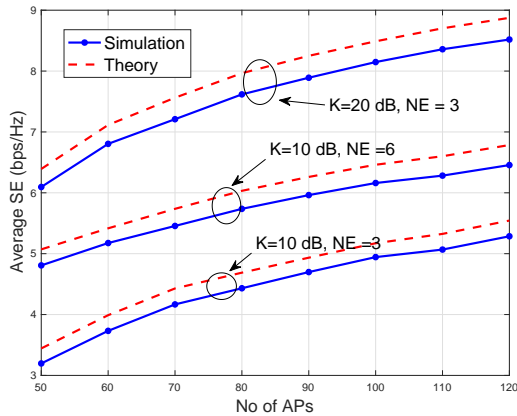


Fig. 8: Average SE vs No of APs.

average SE increases with the NA and NE. This is clear from the fact that as either NA or NE increases, the transmission nulls created towards the sources of interferences become deeper, thereby improving the SINR. The average VSE and the average SE have been plotted vs. NU in Fig. 9 and Fig. 10, respectively for the Rician factor of $K = 10$ dB. The curves are shown for different NA and NE. Observe that the average SE is reduced upon increasing NU, since the SINR is reduced as the number of users is increased. However, in contrast to the average SE, the average VSE initially increases with NU and beyond its maximum it reduces. This is because the reuse factor is increased with NU. Hence, even though the SINR is reduced with NU, the combined effect of the reuse factor and NU results in an increase of the average VSE upto a certain maximum. If however the NU is increased further, the SINR reduction becomes the dominant factor, thereby reducing the average VSE.

Fig. 11-Fig. 13 compare the performance of the cell-based and cell-free architectures in the context of the proposed 3D CBF technique vs. Rician factor K . We consider a pair of 16×16 element arrays for the small cell based structure. The radius of the macro-cell is

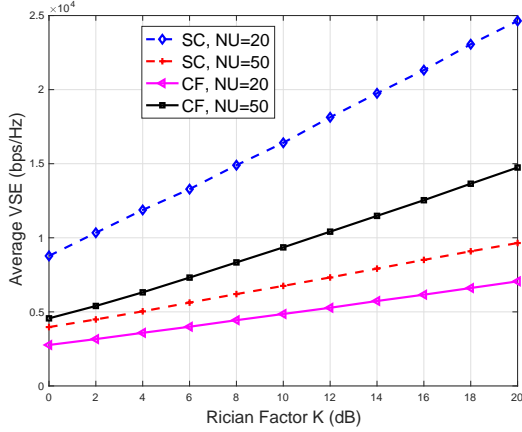


Fig. 11: Average VSE vs Rician Factor K (dB). SC and CF represent small-cell and cell-free configurations, respectively.

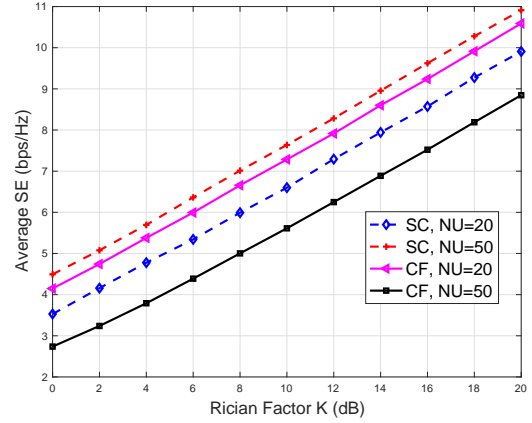


Fig. 12: Average SE vs Rician Factor K (dB). SC and CF represent small-cell and cell-free configurations, respectively.

fixed to 20 m and 30 m , corresponding to 50 and 20 users, respectively. As for the cell-free architecture, the number of APs is fixed to 128, i.e., $NA = 128$ so that 64 APs contributing to each of the CPU. Each AP is constituted by a 4-element array, i.e., $NE = 4$. It may be noted that the array structure of the small-cell configuration as well as of the NA and NE in the cell-free configuration are chosen in such a way that the number of elements per antenna is 256 in both cases. As in the case of the small-cell configuration, in cell-free architecture, the number of users (NU) is set to 50 and 20. Fig. 11, Fig. 12 and Fig. 13 show the average VSE, average SE and average BER vs. the Rician factor, respectively. It can be seen that the performance of the small-cell based architecture is better than that of the cell-free configuration for all the three parameters. The performance difference between the two architectures can be explained by considering the specific antenna structures. In the small-cell configuration, the elements of each antenna are arranged using half-wave-length spacing. By contrast, for the cell-free configuration, the elements are distributed randomly in space. Hence, the antennas in the small-cell based architecture are able to form sharper directional beams and thereby increasing the SINR and improving the performance.

V. CONCLUSIONS

A novel CBF strategy has been proposed for supporting 3D users, which is a 6G system design requirement. The proposed scheme is suitable for numerous applications, especially those related to UAVs and IoT. The proposed technique has been characterized both in small-cell and cell-free wireless topologies. We semi-analytically evaluated the VSE and SE of the proposed scheme and compared them against our simulation results. Furthermore, we also evaluated the BER performance of the proposed scheme. Even though the simulations have been conducted for millimeter wave

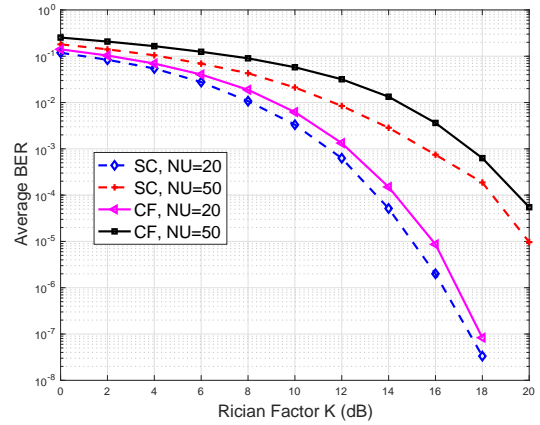


Fig. 13: BER vs Rician Factor K (dB). SC and CF represent small-cell and cell-free configurations, respectively.

frequencies, the methodology is readily applicable for Terahertz (THz) frequencies. Furthermore, we compared the VSE of both the cell-free and the small-cell based architectures and observed that the small-cell based architectures attain better VSE.

Again, we have considered zero forcing JTPC relying on a 3D CBF scheme. An advantage of our PBTBF is that the JTPC vector can be easily computed based on the relative positions of UEs as well as BSs and it dispenses with the channel estimation requirements. Hence, this is eminently suitable for UAV based applications, where the UEs and BSs may be in perpetual movement. A direct extension of this work is to exploit channel impulse response (CIR) based beamforming, which is expected to give better performance as compared to PBTBF, albeit at the cost of an increased computational complexity. An interesting future work item may be to consider the mobility aspects of our scheme, where one has to consider the choice of a suitable modulation scheme, optimal movement trajectory to

maximize the performance and so on. Another promising future work item is to incorporate the 3D CBF techniques in airplane aided communication systems, which has been proposed as a potential technology for improving the coverage probability of 6G systems [39], [64]. In this case, the minimum safety distance between two airplanes, the cooperation strategy among them and many other questions have to be addressed and will be a challenging problem to consider.

APPENDIX A PROOF OF THEOREM 1

Under the conditions of Theorem 1, the average capacity per unit bandwidth can be expressed as:

$$\bar{C}_{h,u} = \int_0^\infty \log_2(1 + \gamma) f_\gamma(\gamma) d\gamma, \quad (13)$$

where $f_\gamma(\gamma)$ is the distribution of γ in (9) and can be estimated as follows. Note that:

$$(\mathbf{e}_{L0} + \mathbf{e}_{R0})^H \mathbf{e}_i \approx 0, \forall i \neq 0, \quad (14)$$

which is a direct consequence of zero-forcing pre-coding. Since both \mathbf{h}_L and \mathbf{h}_R are distributed as $\mathcal{CN}(0, \mathcal{I})$, we have $\mathbf{h}_L + \mathbf{h}_R \sim \mathcal{CN}(0, 2\mathcal{I})$. Hence, it can be deduced that $x_s = \sqrt{P_r} \mathbf{h}_0 \mathbf{e}_0$ and $x_I = \sqrt{P_r} \mathbf{h}_0 \sum_{i=1}^N \mathbf{e}_i + n_0$ are distributed as $\mathcal{CN}(\mu_s, \sigma_s^2)$ and $\mathcal{CN}(0, \sigma_I^2)$, respectively, where $\mu_s = \sqrt{\frac{P_r K}{K+1}} (\mathbf{e}_{L0} + \mathbf{e}_{R0})^H \mathbf{e}_0$, $\sigma_s^2 = \frac{2P_r}{K+1} \|\mathbf{e}_0\|^2$ and $\sigma_I^2 = \frac{2P_r}{K+1} \|\sum_{i=1}^N \mathbf{e}_i\|^2 + \sigma^2$. Now, the distribution of $x = \begin{bmatrix} x_s \\ x_I \end{bmatrix}$ can be obtained from [65, (7)] as:

$$f_x(x) = \frac{2xe^{-k_s^2}}{\sigma_s^2 \sigma_I^2 c_x^2} {}_1F_1\left(2, 1; \frac{x^2 k_s^2}{\sigma_s^2 c_x^2}\right), \quad x > 0, \quad (15)$$

where we have $c_x = \frac{x^2}{\sigma_s^2} + \frac{1}{\sigma_I^2}$. Hence, $\gamma = x^2, x > 0$ is distributed as $f_\gamma(\gamma) = \frac{1}{2\sqrt{\gamma}} f_x(\sqrt{\gamma})$ and is given by:

$$f_\gamma(\gamma) = \frac{e^{-k_s^2}}{\sigma_s^2 \sigma_I^2 c_\gamma^2} {}_1F_1\left(2, 1; \frac{\gamma k_s^2}{\sigma_s^2 c_\gamma^2}\right), \quad \gamma > 0, \quad (16)$$

where $c_\gamma = \frac{\gamma}{\sigma_s^2} + \frac{1}{\sigma_I^2}$. However using [66], we have ${}_1F_1(2, 1; z) = e^z(1+z)$. Therefore, (16) becomes:

$$\begin{aligned} f_\gamma(\gamma) &= \frac{e^{-k_s^2}}{\sigma_s^2 \sigma_I^2} \frac{e^{\frac{\gamma k_s^2}{\sigma_s^2 c_\gamma}}}{c_\gamma^2} \left(1 + \frac{\gamma k_s^2}{\sigma_s^2 c_\gamma}\right) \\ &= \tilde{k} e^{\frac{\gamma k_s^2}{\sigma_s^2 c_\gamma}} \left(\frac{\gamma + \frac{\sigma_s^2}{\sigma_I^2 (1+k_s^2)}}{\left(\gamma + \frac{\sigma_s^2}{\sigma_I^2}\right)^3} \right), \quad \gamma > 0, \end{aligned} \quad (17)$$

where $\tilde{k} = e^{-k_s^2} (1 + k_s^2) \frac{\sigma_s^2}{\sigma_I^2}$ is a constant independent of γ . Let $c_\sigma = \frac{\sigma_s^2}{\sigma_I^2}$. Now, make a change of variable $z = \frac{c_\sigma}{\gamma + c_\sigma}$ in (17) and substitute it into (13). Then we will get:

$$\bar{C}_{h,u} = (1 + k_s^2) I, \quad (18)$$

where the integral I is:

$$I = \int_0^1 \log\left(1 - c_\sigma + \frac{c_\sigma}{z}\right) \left(1 - \frac{k_s^2}{1 + k_s^2} z\right) e^{-k_s^2 z} dz, \quad (19)$$

The expectation (19) can be readily evaluated through tools like *Wolfram Mathematica* and substituted into (18), which will result in (10).

APPENDIX B PROOF OF COROLLARY 1

When we have $k_s \gg 1$ and $c_\sigma \ll k_s^2$, the absolute value of arguments in the exponential integral Ei of (10) is large. Hence, the approximation $Ei(z) \approx \frac{e^z}{z}$ [67] can be used to simplify it, which results in (11).

APPENDIX C

Lemma 1. When the Rician factor satisfies $K \gg 1$, then $k_s \gg 1$.

Proof. Note that:

$$\begin{aligned} k_s &= \frac{|\mu_s|}{\sigma_s} \\ &= \sqrt{\frac{K}{2}} \frac{(\mathbf{e}_{L0} + \mathbf{e}_{R0})^H \mathbf{e}_0}{|\mathbf{e}_0^H \mathbf{e}_0|} \\ &\geq \sqrt{\frac{K}{2}}, \end{aligned} \quad (20)$$

because we have $|(\mathbf{e}_{L0} + \mathbf{e}_{R0})^H \mathbf{e}_0| \geq |\mathbf{e}_0^H \mathbf{e}_0|$. This is because \mathbf{e}_0 is the zero-forcing pre-coding vector in the direction of $(\mathbf{e}_{L0} + \mathbf{e}_{R0})$ and therefore $\|\mathbf{e}_0\| \leq \|\mathbf{e}_{L0} + \mathbf{e}_{R0}\|$. Finally, when $K \gg 1$, then $k_s \gg 1$. \square

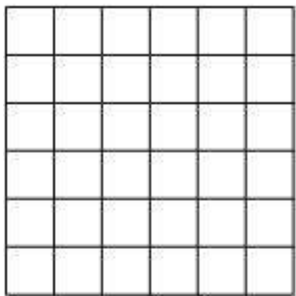
REFERENCES

- [1] K. B. Letaief, W. Chen, Y. Shi, J. Zhang, and Y.-J. A. Zhang, "The roadmap to 6G: AI empowered wireless networks," *IEEE Communications Magazine*, vol. 57, no. 8, pp. 84–90, 2019.
- [2] T. S. Rappaport, Y. Xing, O. Kanhere, S. Ju, A. Madanayake, S. Mandal, A. Alkhateeb, and G. C. Trichopoulos, "Wireless communications and applications above 100 GHz: Opportunities and challenges for 6G and beyond," *IEEE Access*, vol. 7, pp. 78729–78757, 2019.
- [3] I. F. Akyildiz, A. Kak, and S. Nie, "6G and beyond: The future of wireless communications systems," *IEEE Access*, vol. 8, pp. 133995–134030, 2020.
- [4] M. H. Alsharif, A. H. Kelechi, M. A. Albreem, S. A. Chaudhry, M. S. Zia, and S. Kim, "Sixth Generation (6G) Wireless Networks: Vision, Research Activities, Challenges and Potential Solutions," *Symmetry*, vol. 12, no. 4, p. 676, 2020.
- [5] S. Dang, O. Amin, B. Shihada, and M.-S. Alouini, "What should 6G be?," *Nature Electronics*, vol. 3, no. 1, pp. 20–29, 2020.
- [6] I. Bucaille, S. Héthuain, A. Munari, R. Hermenier, T. Rasheed, and S. Allsopp, "Rapidly deployable network for tactical applications: Aerial base station with opportunistic links for unattended and temporary events absolute example," in *MIL-COM 2013-2013 IEEE military communications conference*, pp. 1116–1120, IEEE, 2013.
- [7] M. Mozaffari, W. Saad, M. Bennis, Y.-H. Nam, and M. Debbah, "A tutorial on UAVs for wireless networks: Applications, challenges, and open problems," *IEEE Communications Surveys & Tutorials*, vol. 21, no. 3, pp. 2334–2360, 2019.

- [8] M. Mozaffari, A. T. Z. Kasgari, W. Saad, M. Bennis, and M. Debbah, "Beyond 5G with UAVs: Foundations of a 3D wireless cellular network," *IEEE Transactions on Wireless Communications*, vol. 18, no. 1, pp. 357–372, 2018.
- [9] B. Li, Z. Fei, and Y. Zhang, "UAV communications for 5G and beyond: Recent advances and future trends," *IEEE Internet of Things Journal*, vol. 6, no. 2, pp. 2241–2263, 2018.
- [10] T.-Z. Xiang, G.-S. Xia, and L. Zhang, "Mini-unmanned aerial vehicle-based remote sensing: techniques, applications, and prospects," *IEEE Geoscience and Remote Sensing Magazine*, vol. 7, no. 3, pp. 29–63, 2019.
- [11] P. Partinevelos, D. Chatziparaschis, D. Trigkakis, and A. Tripolitisiotis, "A novel UAV-assisted positioning system for GNSS-denied environments," *Remote Sensing*, vol. 12, no. 7, p. 1080, 2020.
- [12] D. Bamburay, "Drones: Designed for product delivery," *Design Management Review*, vol. 26, no. 1, pp. 40–48, 2015.
- [13] S. Hosseinalipour, A. Rahmati, H. Dai, et al., "Energy-aware stochastic UAV-assisted surveillance," *IEEE Transactions on Wireless Communications*, 2020.
- [14] W. Saad, M. Bennis, and M. Chen, "A vision of 6G wireless systems: Applications, trends, technologies, and open research problems," *IEEE network*, vol. 34, no. 3, pp. 134–142, 2019.
- [15] S. M. Razavizadeh, M. Ahn, and I. Lee, "Three-dimensional beamforming: A new enabling technology for 5G wireless networks," *IEEE Signal Processing Magazine*, vol. 31, no. 6, pp. 94–101, 2014.
- [16] W. H. Chin, Z. Fan, and R. Haines, "Emerging technologies and research challenges for 5G wireless networks," *IEEE Wireless Communications*, vol. 21, no. 2, pp. 106–112, 2014.
- [17] A. Zanella, N. Bui, A. Castellani, L. Vangelista, and M. Zorzi, "Internet of things for smart cities," *IEEE Internet of Things Journal*, vol. 1, no. 1, pp. 22–32, 2014.
- [18] J. Gubbi, R. Buyya, S. Marusic, and M. Palaniswami, "Internet of Things (IoT): A vision, architectural elements, and future directions," *Future Generation Computer Systems*, vol. 29, no. 7, pp. 1645–1660, 2013.
- [19] Z. Dawy, W. Saad, A. Ghosh, J. G. Andrews, and E. Yacoub, "Toward massive machine type cellular communications," *IEEE Wireless Communications*, vol. 24, no. 1, pp. 120–128, 2016.
- [20] S.-Y. Lien, K.-C. Chen, and Y. Lin, "Toward ubiquitous massive accesses in 3GPP machine-to-machine communications," *IEEE Communications Magazine*, vol. 49, no. 4, pp. 66–74, 2011.
- [21] L. Lu, G. Y. Li, A. L. Swindlehurst, A. Ashikhmin, and R. Zhang, "An overview of massive MIMO: Benefits and challenges," *IEEE journal of selected topics in signal processing*, vol. 8, no. 5, pp. 742–758, 2014.
- [22] X. Gao, O. Edfors, F. Rusek, and F. Tufvesson, "Massive MIMO performance evaluation based on measured propagation data," *IEEE Transactions on Wireless Communications*, vol. 14, no. 7, pp. 3899–3911, 2015.
- [23] E. G. Larsson, O. Edfors, F. Tufvesson, and T. L. Marzetta, "Massive MIMO for next generation wireless systems," *IEEE Communications Magazine*, vol. 52, no. 2, pp. 186–195, 2014.
- [24] S. Zhou, M. Zhao, X. Xu, J. Wang, and Y. Yao, "Distributed wireless communication system: a new architecture for future public wireless access," *IEEE Communications Magazine*, vol. 41, no. 3, pp. 108–113, 2003.
- [25] M. K. Karakayali, G. J. Foschini, and R. A. Valenzuela, "Network coordination for spectrally efficient communications in cellular systems," *IEEE Wireless Communications*, vol. 13, no. 4, pp. 56–61, 2006.
- [26] W. Choi and J. G. Andrews, "Downlink performance and capacity of distributed antenna systems in a multicell environment," *IEEE Transactions on Wireless Communications*, vol. 6, no. 1, pp. 69–73, 2007.
- [27] R. Irmer, H. Droste, P. Marsch, M. Grieger, G. Fettweis, S. Brueck, H.-P. Mayer, L. Thiele, and V. Jungnickel, "Coordinated multipoint: Concepts, performance, and field trial results," *IEEE Communications Magazine*, vol. 49, no. 2, pp. 102–111, 2011.
- [28] X. Hong, Y. Jie, C.-X. Wang, J. Shi, and X. Ge, "Energy-spectral efficiency trade-off in virtual MIMO cellular systems," *IEEE Journal on Selected Areas in Communications*, vol. 31, no. 10, pp. 2128–2140, 2013.
- [29] D. Castanheira and A. Gameiro, "Distributed antenna system capacity scaling [coordinated and distributed MIMO]," *IEEE Wireless Communications*, vol. 17, no. 3, pp. 68–75, 2010.
- [30] H. Q. Ngo, A. Ashikhmin, H. Yang, E. G. Larsson, and T. L. Marzetta, "Cell-free massive MIMO versus small cells," *IEEE Transactions on Wireless Communications*, vol. 16, no. 3, pp. 1834–1850, 2017.
- [31] M.-S. Alouini and A. J. Goldsmith, "Area spectral efficiency of cellular mobile radio systems," *IEEE Transactions on Vehicular Technology*, vol. 48, no. 4, pp. 1047–1066, 1999.
- [32] C. Li, J. Zhang, J. G. Andrews, and K. B. Letaief, "Success probability and area spectral efficiency in multiuser MIMO HetNets," *IEEE Transactions on Communications*, vol. 64, no. 4, pp. 1544–1556, 2016.
- [33] M. Ding, D. López-Pérez, G. Mao, P. Wang, and Z. Lin, "Will the area spectral efficiency monotonically grow as small cells go dense?," in *2015 IEEE Global Communications Conference (GLOBECOM)*, pp. 1–7, IEEE, 2015.
- [34] Y. Xin, D. Wang, J. Li, H. Zhu, J. Wang, and X. You, "Area spectral efficiency and area energy efficiency of massive MIMO cellular systems," *IEEE Transactions on Vehicular Technology*, vol. 65, no. 5, pp. 3243–3254, 2015.
- [35] L. Zhang, H.-C. Yang, and M. O. Hasna, "Generalized area spectral efficiency: An effective performance metric for green wireless communications," *IEEE Transactions on Communications*, vol. 62, no. 2, pp. 747–757, 2014.
- [36] M. R. Rahaman Khan and V. Tuzlukov, "Null-steering beamforming for cancellation of co-channel interference in CDMA wireless communication system," in *2010 4th International Conference on Signal Processing and Communication Systems*, pp. 1–5, IEEE, 2010.
- [37] J. Litva and T. K. Lo, *Digital beamforming in wireless communications*. Artech House, Inc., 1996.
- [38] S. Yoo, S. Kim, D. H. Youn, and C. Lee, "Multipath mitigation technique using null-steering beamformer for positioning system," in *The 57th IEEE Semiannual Vehicular Technology Conference, 2003. VTC 2003-Spring*, vol. 1, pp. 602–605, IEEE, 2003.
- [39] M. Srinivasan, S. Gopi, S. Kalyani, X. Huang, and L. Hanzo, "Airplane-aided integrated next-generation networking," *arXiv preprint arXiv:2101.00566*, 2021.
- [40] P. Liu, M. Di Renzo, and A. Springer, "Line-of-sight spatial modulation for indoor mmwave communication at 60 GHz," *IEEE Transactions on Wireless Communications*, vol. 15, no. 11, pp. 7373–7389, 2016.
- [41] T. S. Rappaport, G. R. MacCartney, M. K. Samimi, and S. Sun, "Wideband millimeter-wave propagation measurements and channel models for future wireless communication system design," *IEEE Transactions on Communications*, vol. 63, no. 9, pp. 3029–3056, 2015.
- [42] R. Xu, Z. Zhong, and J.-M. Chen, "Approximation to the capacity of Rician fading MIMO channels," in *VTC Spring 2009-IEEE 69th Vehicular Technology Conference*, pp. 1–5, IEEE, 2009.
- [43] H. L. Van Trees, *Optimum array processing: Part IV of detection, estimation, and modulation theory*. John Wiley & Sons, 2004.
- [44] W. Qingqing and Z. Rui, "Towards smart and reconfigurable environment: Intelligent reflecting surface aided wireless network," *arXiv preprint arXiv:1905.00152*, 2019.
- [45] L. Dai, B. Wang, M. Wang, X. Yang, J. Tan, S. Bi, S. Xu, F. Yang, Z. Chen, M. Di Renzo, C.-B. Chae, and L. Hanzo, "Reconfigurable intelligent surface-based wireless communications: Antenna design, prototyping, and experimental results," *IEEE Access*, vol. 8, pp. 45913–45923, 2020.
- [46] M. Di Renzo, M. Debbah, D.-T. Phan-Huy, A. Zappone, M.-S. Alouini, C. Yuen, V. Sciancalepore, G. C. Alexandropoulos, J. Hoydis, H. Gacanin, J. d. Rosny, A. Bounceur, G. Lerosee, and M. Fink, "Smart radio environments empowered by reconfigurable AI meta-surfaces: an idea whose time has come," *EURASIP Journal on Wireless Communications and Networking*, vol. 2019, no. 1, pp. 1–20, 2019.
- [47] W. Yan, X. Yuan, and X. Kuai, "Passive beamforming and information transfer via large intelligent surface," *IEEE Wireless Communications Letters*, vol. 9, no. 4, pp. 533–537, 2019.
- [48] X. Yu, D. Xu, and R. Schober, "MISO wireless communication systems via intelligent reflecting surfaces : (Invited paper)," in

- 2019 IEEE/CIC International Conference on Communications in China (ICCC), pp. 735–740, Aug 2019.
- [49] Y. Han, W. Tang, S. Jin, C. Wen, and X. Ma, “Large intelligent surface-assisted wireless communication exploiting statistical CSI,” *IEEE Transactions on Vehicular Technology*, vol. 68, pp. 8238–8242, Aug 2019.
 - [50] C. Huang, A. Zappone, G. C. Alexandropoulos, M. Debbah, and C. Yuen, “Reconfigurable intelligent surfaces for energy efficiency in wireless communication,” *IEEE Transactions on Wireless Communications*, vol. 18, pp. 4157–4170, Aug 2019.
 - [51] C. Huang, G. C. Alexandropoulos, A. Zappone, M. Debbah, and C. Yuen, “Energy efficient multi-user MISO communication using low resolution large intelligent surfaces,” in *2018 IEEE Globecom Workshops (GC Wkshps)*, pp. 1–6, IEEE, 2018.
 - [52] J. Chen, Y. Liang, Y. Pei, and H. Guo, “Intelligent reflecting surface: A programmable wireless environment for physical layer security,” *IEEE Access*, vol. 7, pp. 82599–82612, 2019.
 - [53] C. Pan, H. Ren, K. Wang, W. Xu, M. ElKashlan, A. Nallanathan, and L. Hanzo, “Multicell MIMO communications relying on intelligent reflecting surfaces,” *IEEE Transactions on Wireless Communications*, vol. 19, no. 8, pp. 5218–5233, 2020.
 - [54] E. Basar, “Reconfigurable intelligent surface-based index modulation: A new beyond MIMO paradigm for 6G,” *IEEE Transactions on Communications*, vol. 68, no. 5, pp. 3187–3196, 2020.
 - [55] S. Gopi, S. Kalyani, and L. Hanzo, “Intelligent reflecting surface assisted beam index-modulation for millimeter wave communication,” *IEEE Transactions on Wireless Communications*, pp. 1–1, 2020.
 - [56] S. N. Alam and Z. J. Haas, “Coverage and connectivity in three-dimensional networks,” in *Proceedings of the 12th annual international conference on Mobile computing and networking*, pp. 346–357, 2006.
 - [57] R. L. Graham, D. E. Knuth, and O. Patashnik, *Concrete mathematics: a foundation for computer science*. Addison-Wesley, 2 ed., 1994.
 - [58] H. Yan, S. Ramesh, T. Gallagher, C. Ling, and D. Cabric, “Performance, power, and area design trade-offs in millimeter-wave transmitter beamforming architectures,” *IEEE Circuits and Systems Magazine*, vol. 19, no. 2, pp. 33–58, 2019.
 - [59] S. Nie, G. R. MacCartney, S. Sun, and T. S. Rappaport, “28 GHz and 73 GHz signal outage study for millimeter wave cellular and backhaul communications,” in *2014 IEEE International Conference on Communications (ICC)*, pp. 4856–4861, IEEE, 2014.
 - [60] S. A. Rao, N. Kumar, et al., “Modeling and link budget estimation of directional mmwave outdoor environment for 5G,” in *2019 European Conference on Networks and Communications (EuCNC)*, pp. 106–111, IEEE, 2019.
 - [61] G. R. MacCartney and T. S. Rappaport, “73 GHz millimeter wave propagation measurements for outdoor urban mobile and backhaul communications in New York City,” in *2014 IEEE International Conference on Communications (ICC)*, pp. 4862–4867, IEEE, 2014.
 - [62] G. R. MacCartney and T. S. Rappaport, “Rural macrocell path loss models for millimeter wave wireless communications,” *IEEE Journal on selected areas in communications*, vol. 35, no. 7, pp. 1663–1677, 2017.
 - [63] C. A. Balanis, *Antenna theory: analysis and design*. John Wiley & sons, 2016.
 - [64] X. Huang, J. A. Zhang, R. P. Liu, Y. J. Guo, and L. Hanzo, “Airplane-Aided Integrated Networking for 6G Wireless: Will It Work?,” *IEEE Vehicular Technology Magazine*, vol. 14, no. 3, pp. 84–91, 2019.
 - [65] S. Nadarajah and H. S. Kwong, “A note on “On the ratio of independent complex Gaussian random variables”,,” *Multi-dimensional Systems and Signal Processing*, vol. 29, no. 4, pp. 1839–1843, 2018.
 - [66] Wolfram Research, “Hypergeometric1f1.” [Online]. Available: <http://functions.wolfram.com/HypergeometricFunctions/Hypergeometric1F1/03/02/10/0015/>. Last visited on 17/9/2020.
 - [67] Wolfram Research, “Expintegratei.” [Online]. Available: <http://functions.wolfram.com/GammaBetaErf/ExpIntegralEi/06/02/0006/>. Last visited on 04/11/2020.

A1



θ_1

UE2



UE0



UE3



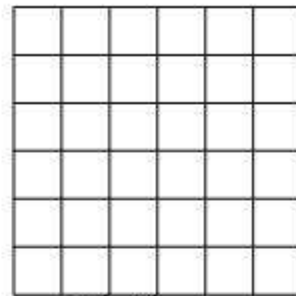
UE1



UE4

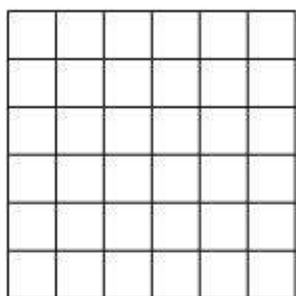


A2



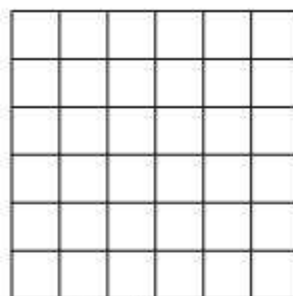
θ_2

A1



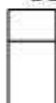
θ_1

A2

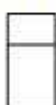


θ_2

UE0



UE2



UE1

